




Probing the Dipole of the Diffuse Gamma-Ray Background

A. Kashlinsky^{1,2,3} , F. Atrio-Barandela⁴ , and C. S. Shrader^{5,6} ¹ Code 665, Observational Cosmology Lab, NASA Goddard Space Flight Center, Greenbelt, MD 20771, USA; Alexander.Kashlinsky@nasa.gov
² SSAI, Lanham, MD 20770, USA³ Department of Astronomy, University of Maryland, College Park, MD 20742, USA⁴ Department of Fundamental Physics, University of Salamanca, E-37008 Salamanca, Spain⁵ Code 661, Astroparticle Physics Lab., NASA Goddard Space Flight Center, Greenbelt, MD 20771, USA⁶ Department of Physics, Catholic University of America, USA

Received 2023 September 7; revised 2023 September 27; accepted 2023 September 28; published 2024 January 10

Abstract

We measured the dipole of the diffuse γ -ray background (DGB), identifying a highly significant time-independent signal coincidental with that of the Pierre Auger UHECR. The DGB dipole is determined from flux maps in narrow energy bands constructed from 13 yr of observations by the Large Area Telescope (LAT) of the Fermi satellite. The γ -ray maps were clipped iteratively of sources and foregrounds similar to that done for the cosmic infrared background. The clipped narrow energy band maps were then assembled into one broad energy map out to the given energy starting at $E = 2.74$ GeV, where the LAT beam falls below the sky's pixel resolution. Next we consider cuts in Galactic latitude and longitude to probe residual foreground contaminations from the Galactic plane and center. In the broad energy range $2.74 < E \leq 115.5$ GeV, the measured dipoles are stable with respect to the various Galactic cuts, consistent with an extragalactic origin. The γ -ray sky's dipole/monopole ratio is much greater than that expected from the DGB clustering component and the Compton–Getting effect origin with reasonable velocities. At $\simeq(6.5\text{--}7)\%$ it is similar to the Pierre Auger UHECRs with $E_{\text{UHECR}} \geq 8$ EeV, pointing to a common origin of the two dipoles. However, the DGB flux associated with the found DGB dipole reaches parity with that of the UHECR around $E_{\text{UHECR}} \leq 1$ EeV, perhaps arguing for a non-cascading mechanism if the DGB dipole were to come from the higher-energy UHECRs. The signal-to-noise ratio of the DGB dipole is largest in the 5–30 GeV range, possibly suggesting the γ -photons at these energies are the ones related to cosmic rays.

Unified Astronomy Thesaurus concepts: [High-energy cosmic radiation \(731\)](#); [Ultra-high-energy cosmic radiation \(1733\)](#)

1. Introduction

The energy spectrum of the diffuse γ -ray background (DGB) is known accurately from Fermi Large Area Telescope (LAT) measurements: $F_{\text{DGB}} \equiv E^2 dN/dE = 4 \times 10^{-7} \left(\frac{E}{\text{GeV}}\right)^{-\gamma} \text{ GeV cm}^{-2} \text{ s}^{-1} \text{ sr}^{-1}$ at $0.1 \lesssim E(\text{GeV}) \lesssim 100$ with $\gamma \simeq 0.35$ (Ackermann et al. 2012b, 2015). The power of its angular anisotropies have been measured to be flat (white noise) at $C_\ell/F_{\text{DGB}}^2 \simeq (8\text{--}9) \times 10^{-6} \text{ sr}$ out to $\theta \sim 7^\circ$ ($\ell > 50$; Ackermann et al. 2012a, 2018). The DGB dipole has not yet been measured although it would carry important cosmological information arising from one of the following three origins: (1) The Compton–Getting (Compton & Getting 1935) effect from the Sun's motion generates an amplified dipole over that of the cosmic microwave background (CMB), assuming the latter is entirely kinematic at $V_{\text{CMB}} = 370 \text{ km s}^{-1}$ (Kogut et al. 1993). Since $E^{-2} dN/dE$ is Lorentz invariant (Peebles & Wilkinson 1968), the dimensionless kinematic DGB dipole would be $\mathcal{D}_{\text{DGB}} = (4 + \gamma) \frac{V}{c} \simeq 0.56\% (V/V_{\text{CMB}})$, an amplification that is comparable (Maoz 1994) to that for cosmic rays (CRs; Kachelrieß & Serpico 2006) and the cosmic infrared background (CIB; Kashlinsky 2005a; Kashlinsky & Atrio-Barandela 2022). (2) The clustering (measured to have white noise angular spectrum) component dipole from the unresolved DGB sources would be $\simeq \sqrt{C_\ell}/F_{\text{DGB}} \simeq 0.25\%$ using

measurements from Ackermann et al. (2012b, 2018) and also here. (3) The Fermi-LAT photons may trace other cosmic structures, such as those implied by the UHECR Pierre Auger dipole of $\simeq(6.5\text{--}7)\% F_{\text{DGB}}$ (Pierre Auger Collaboration et al. 2017; Aab et al. 2020a).

In proper interpretation, the DGB dipole must be described not only with amplitude but also with its direction. Here, however, fine measurements at high signal-to-noise ratio (S/N) are required since the directional uncertainty in the limit of $S/N > 1$ is $\Delta\theta \simeq \sqrt{2} (S/N)^{-1} \text{ rad}$ (Fixsen & Kashlinsky 2011), and only CMB dipole, probed at $S/N > 200$ (Kogut et al. 1993; Fixsen et al. 1994), currently allows high-precision directional determination.

We present the first measurement of the source-subtracted flux dipole over [3–100] GeV using Fermi 13 yr data. We assemble the UltraClean Fermi data set using HEALPix with $N_{\text{side}} = 128$ (Górski et al. 2005) from the 13 yr all-sky observations at narrow energy bands. After removing known sources, each E -map is cleaned of the ecliptic plane, the Galactic plane, and remaining Galactic and extragalactic sources, structured foregrounds, and noise excursions via a standard iterative procedure used in CIB work (see, e.g., reviews by Kashlinsky 2005a; Kashlinsky et al. 2018). Then, possible remaining Galaxy emissions are further removed with progressive Galactic cuts in $(l_{\text{Gal}}, b_{\text{Gal}})$. The clipped, narrow E -maps were assembled into broad bands of increasing upper energy and the residual map dipoles evaluated for each situation. We find a robust remaining source-subtracted dipole that is highly statistically significant and independent of further

Galaxy and source removal, consistent with an extragalactic origin. The signal appears stable in time for at least 6 yr. The relative amplitude of the dipole is (6–7)%, which is much higher than could come from the DGB source clustering component and also higher than any kinematic Compton–Getting component, unless the local velocity is $V \gtrsim 3000 \text{ km s}^{-1}$. However, the relative dipole amplitude coincides with that of the UHECR dipole from Pierre Auger Observatory (Pierre Auger Collaboration et al. 2017; Aab et al. 2020a), which we interpret as indicative of a common origin of the [3–100] GeV photons here and the UHECR.

2. Fermi-LAT Data and Processing

The Fermi-LAT is a pair-conversion telescope covering the nominal [0.1–1000] GeV energy range (Atwood et al. 2009). It is operated as a sky-survey instrument, having both a wide field of view, $\sim 2 \text{ sr}$, and large effective area: $\sim 0.7 \text{ m}^2$ for $\sim 1 \text{ GeV}$ photons at near normal incidence. The telescope is comprised of a 4×4 assembly of modules that each consists of a tracker and calorimeter to record information needed to reconstruct photon direction and energy. The instrument is enclosed by an active anticoincidence system that allows the onboard electronics to reject charged particle events.

We selected data taken at the start of scientific operations, continuing through the end of mission Cycle 13, specifically, all the weekly photon files 2008 August 31–2021 September 1. We used the weekly photon files resulting from the latest reprocessing, P8R3⁷ and the front-plus-back converting events. To limit contamination from γ -rays scattered from the Earth’s atmosphere, a selection cut was applied to remove data taken when the LAT boresight rocked to $>52^\circ$ with respect to the zenith. The selection cuts resulting from this reprocessing significantly reduce the occurrence of CR-induced spurious (i.e., non-photon) events and importantly, remove residual-associated anisotropies (Bruel et al. 2018). It should also be noted that these spurious events can introduce anisotropies in large- or all-sky analyses. This is due to both noninteracting heavy ions and to CR electrons leaking through the ribbons of the anticoincidence detector, the latter source being responsible for the background anisotropy. We also excluded any time interval when the LAT was not in survey mode. To minimize potential contamination from CR-induced events in the detector, we selected the “UltraClean” event selection cut and the corresponding instrument-response function.

The possible effects on the measured DGB dipole by emissions emanating from within the solar system are demonstrated below to be negligible.

Our analysis benefits from including as many celestial photons as possible, but bright sources above our latitude cuts that are in relatively close proximity would likely introduce anisotropies. Thus we exclude emission from the remaining brightest 3000+ sources from the fourth Fermi Gamma-Ray Lat (4FGL) catalog (Abdollahi et al. 2022), then employing the clipping procedure as detailed below.

The 1–100 GeV energy γ -ray sky at low Galactic latitudes is dominated by diffuse emissions from interactions of CRs with the interstellar medium as well as with the Milky Way radiation fields. While these foreground emissions, which have been studied extensively (Ackermann et al. 2012b), provide a useful diagnostic tool to study the interstellar medium and CR

propagation, they are an impediment to large-scale extragalactic studies. The Galactic latitude b_{Gal} and longitude l_{Gal} cuts employed in our analysis partially remove the effects of these structured foregrounds on our analysis. We assess further effects by making incremental cuts at $|b_{\text{Gal}}| > 20^\circ, 30^\circ, 45^\circ$ and 30° and at $45^\circ \leq l_{\text{Gal}} \leq 330^\circ, 315^\circ$, and also by removing the ecliptic plane and then recomputing the dipole.

We apply the clipping procedure well known and commonly used in the source-subtracted CIB studies since the COBE/DIRBE, later refined for and further tested in the various 2MASS, Spitzer, and Euclid work (see reviews in Kashlinsky 2005a; Kashlinsky et al. 2018). The method isolates iteratively the pixels with photons exceeding a given threshold of $N_{\text{phot}}(l_{\text{Gal}}, b_{\text{Gal}}) \geq \langle N_{\text{phot}} \rangle + N_{\text{cut}} \sigma(N_{\text{phot}})$, removing here the entire beam at 95% c.l. around the pixels identified in the given iteration and proceeds until no more such excursions are found at the given N_{cut} . Typically up to ten iterations were needed to converge, and the results are insensitive at $N_{\text{cut}} \leq 4$. Of course, the method should be applied to as narrow bands as possible, especially for the γ -ray sky where adjacent energies often trace different sources. Figures 5 and 6 show the commonality of the remaining photons for the unclipped and clipped maps, demonstrating the efficiency and necessity of clipping. After clipping, most remaining pixels starting already around (3–5) GeV trace different sources at two adjacent bands, and most of the sky becomes progressively darker (no photons in each pixel) at narrow energy bands, as expected. Next we combine different bands into one broader band map and then evaluate the dipoles and the mean remaining flux.

Figure 1(a) shows the number of photons left in each band after the procedures. The horizontal green line in Figure 1(a) shows the pixel area (right vertical axis), and the green stars mark the 95% LAT beam area that falls below our pixel resolution at $E \gtrsim 3 \text{ GeV}$. Those remaining after clipping γ -ray sources are unresolved at this resolution.

We therefore restrict our dipole DGB analysis to $E > 2.74 \text{ GeV}$. The clipped maps at narrow energy bands are then coadded up to $E = 115 \text{ GeV}$. Figure 1(b) shows the consistency of the histograms of the assembled source-subtracted maps for various $|b_{\text{Gal}}|$ -cuts and $30^\circ \leq l_{\text{Gal}} \leq 330^\circ$. The resultant clipped map assembled over $2.74 \leq E(\text{GeV}) \leq 115$ is shown in Figure 2; the symbols are explained below.

3. Dipole Results

Computations of the multipole expansion of source-subtracted, band-added maps were done with standard HEALPix routines: dipole with REMOVE_DIPOLE and power spectrum with ANAFast developed with singular-value decomposition (Górski et al. 2005).

The dipole from the clipped maps is shown with circles in Figure 3. The dashed lines of three colors in Figure 1(b) show the mean flux in the clipped maps of three values of b_{cut} , and the solid lines of the same color show the flux dispersion of each map. The flux dispersion is $\sigma_F \sim 0.8 \times 10^{-7} \text{ GeV cm}^{-2} \text{ s}^{-1} \text{ sr}^{-1}$, which introduces random dipole uncertainty in each of the three components over a map of N_{pix} pixels of $\sim \sigma_F / \sqrt{N_{\text{pix}}}$. For the dipole amplitude, the uncertainty will be $\sqrt{3} \sigma_F \sim 5 \times 10^{-10} \sqrt{N_{\text{pix}}} / 10^5 \text{ GeV cm}^{-2} \text{ s}^{-1} \text{ sr}^{-1}$, which shows that the dipoles found in Figure 3 are statistically significant. A more accurate estimate of the statistical error can be done by bootstrap. We generated 1000 simulated maps by assigning to each point on

⁷ <https://fermi.gsfc.nasa.gov/ssc/data/access/>

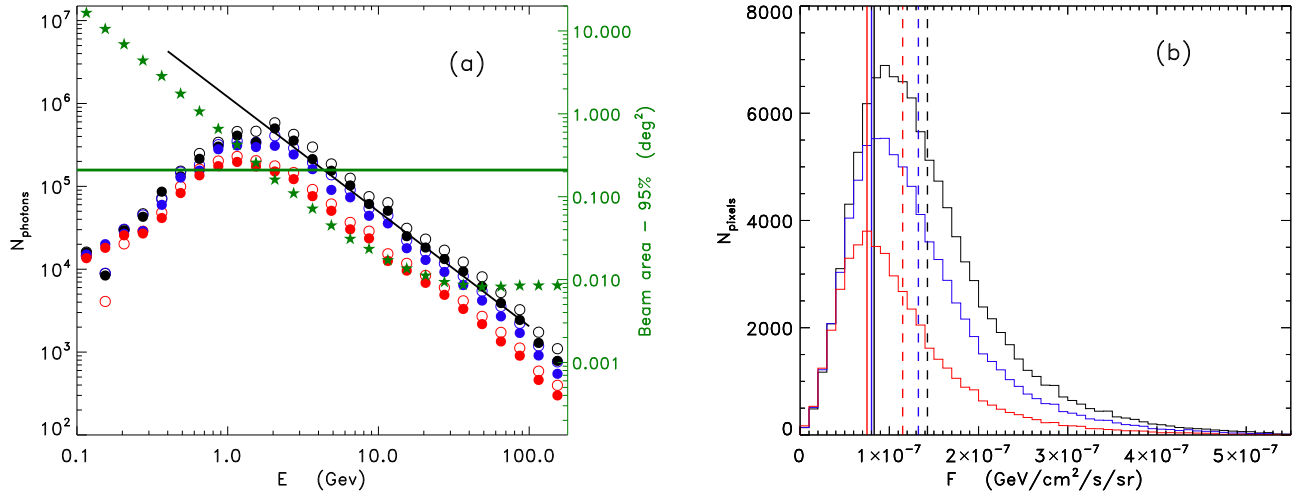


Figure 1. (a) Total number of photons in each narrow band is marked with filled circles. Black, blue, and red circles correspond to $|b_{\text{Gal}}| \geq 20^\circ$, 30° , and 45° while filled (open) circles corresponds to $0 \leq l_{\text{Gal}} \leq 360^\circ$ ($30^\circ \leq l_{\text{Gal}} \leq 330^\circ$). The LAT beam is shown with green stars for the values displayed on the right vertical axis. The horizontal thick green solid line marks the pixel area for $N_{\text{side}} = 128$. The slope of the DGB is marked with black solid line. (b) Flux histograms for $2.74 \leq E(\text{GeV}) \leq 115$ and $30^\circ \leq l_{\text{Gal}} \leq 330^\circ$ with black/blue/red corresponding to $|b_{\text{Gal}}| \geq 20^\circ$, 30° , and 45° . Dashed and solid vertical lines of three colors mark the mean flux and flux dispersion of each map.

$$2.74 \leq E(\text{GeV}) \leq 115.5$$

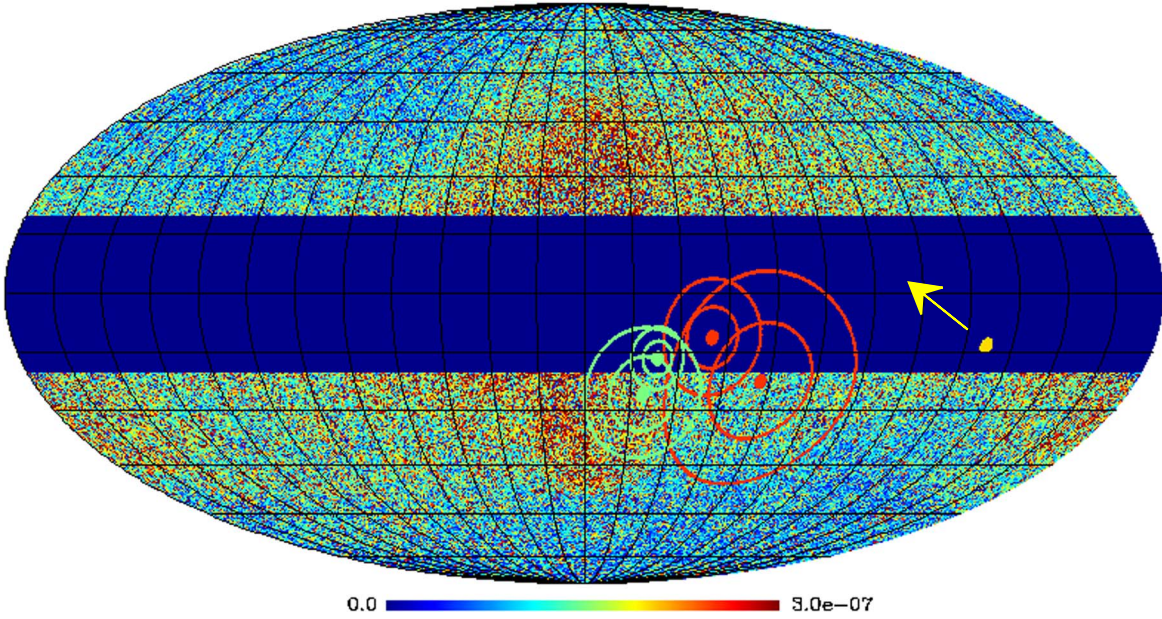


Figure 2. The source-subtracted LAT maps coadded from 2.74 to 115 GeV. The displayed sky is masked for $|b_{\text{Gal}}| \leq 20^\circ$. The coordinate grid is marked every 15° . The DGB dipole directions are plotted for the $45^\circ \leq l_{\text{Gal}} \leq 315^\circ$, $|b_{\text{Gal}}| \geq 45^\circ$ with red colors and the $30^\circ \leq l_{\text{Gal}} \leq 330^\circ$, $|b_{\text{Gal}}| \geq 30^\circ$ with green colors. The two contours in each case correspond to 1σ and 2σ (68% and 95%) dipole uncertainties. The size of each contour decreases as it should when larger sky area is considered. The smaller/narrower contours indicate the directions and uncertainties of the 13 yr assembled map shown here. The larger/broader contours show the same once the $(A-B)/2$ dipoles have been subtracted. The yellow arrow indicates the tentative position of the Pierre Auger dipole prior to the deflection by the modeled Galactic magnetic field. The Pierre Auger UHECR dipole is marked with the yellow spot and its 68% directional uncertainty is $\sim 15^\circ$. The map with the ecliptic plane masked out with $|\beta_{\text{Ecl}}| \leq 5^\circ$ is shown in Figure 7.

the unmasked regions of the sky a value extracted at random from the flux map of 13 yr of data. All data points were given the same probability. Following bootstrap standard practice, the selected values were not removed. Once a random map j was generated, its dipole \mathbf{d}^j was computed using the HEALPix `remove_dipole` routine. The mean of each dipole component is zero, and its dispersion is a measure of the statistical error. The ratio of the signal to its statistical uncertainty is largest in the energy range $\sim(5-30)$ GeV.

Next, we computed the statistical uncertainty in the dipole direction using the errors σ_i by generating $k = 10^4$ Gaussian distributed vectors \mathbf{d}^k about the dipole components D_i measured from the 13 yr flux map, $d_i^k = D_i + r_i^k \sigma_i$ with r_i^k Gaussian random numbers with zero mean and unit variance. These bootstrap error estimates do not probe the time-variable component of the dipole that might be present in the data from instrument noise, systematics, or genuine γ -ray variability.

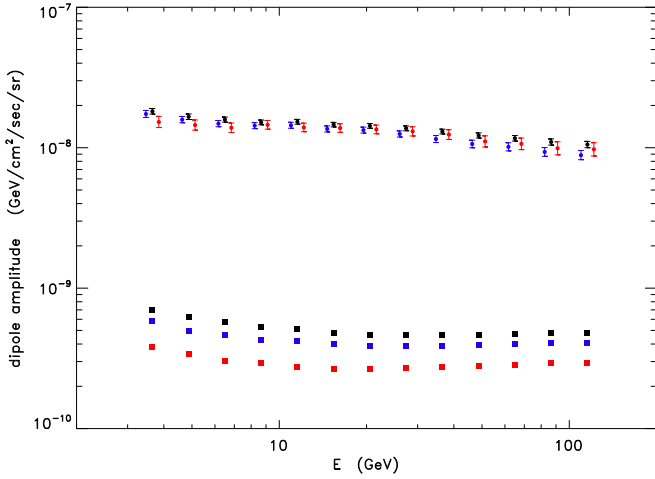


Figure 3. Black, blue, and red colors mark $|b_{\text{Gal}}| \geq 20^\circ, 30^\circ, 45^\circ$ for $30^\circ \leq l_{\text{Gal}} \leq 330^\circ$. The points are slightly shifted at each E for clearer display, and the configuration of $45^\circ \leq l_{\text{Gal}} \leq 315^\circ$ is not shown to avoid clutter (it is shown in Figure 4). The square root of the clustering mean power over $\ell \geq 20$ from Figure 3 are shown with squares. The dipoles in the source-subtracted 13 yr maps are shown with filled circles with the 68% uncertainties.

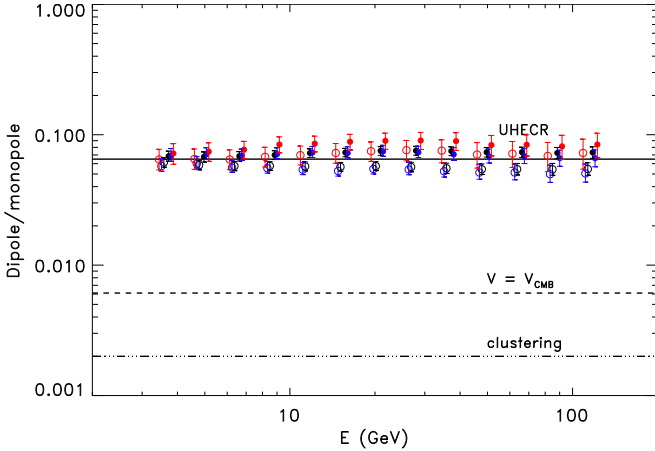


Figure 4. Dimensionless dipole in the same notations as in Figure 3. In addition to the numbers in Figure 3, red/blue/black open circles denote the configurations with $45^\circ \leq l_{\text{Gal}} \leq 315^\circ$ and $2.74 < E(\text{GeV}) < 115$ slightly shifted in E for clear viewing (this is not shown in the earlier figure to avoid overcrowding—all the numbers are consistent with what is shown here). The dimensionless dipoles from CRs (UHECR) at 6.5%, Compton-Getting amplified CMB dipole, and clustering component are marked with horizontal lines. Removing the ecliptic plane, as discussed in the Appendix, further reduces the scatter—see Figure 8. The statistical uncertainties are shown at 95% c.i.

For estimating the time variations and noise in the maps, we assembled two time-separated subsets of data: A for years 1–6 and B for years 7–12 with the odd year 13 left out temporarily for this task. Each of the two 6 yr time intervals are longer than the typical variability timescales of γ -ray sources. The masks from the clipping of sources and Galaxy for the full 13 yr map in $(b_{\text{Gal}}, l_{\text{Gal}})$ are applied to each subset, and the narrow E -bands are then coadded to produce the 13 yr wide band maps going from $E_0 = 2.74$ GeV to the given E up to $E = 115$ GeV. Then, similar to the by-now standard CMB (Smoot et al. 1992; Bennett et al. 1996) and CIB (Arendt et al. 2010; Kashlinsky et al. 2012) noise power processing, the noise properties are computed from the $(A - B)/2$ maps, masked in the same way as the combined 13 yr data. The resultant noise map is shown in Figure 9, and the dipole amplitudes of the 13 yr and $(A - B)/2$ and dipole powers

are compared in Figure 11. Figure 10, left panel, displays the histograms in the time-differenced maps with the ecliptic plane masked out, showing the standard deviations using 12 yr data of $\sigma_{F,(A-B)/2} \sim 1.2 \times 10^{-7} \text{ GeV cm}^{-2} \text{ s}^{-1} \text{ sr}^{-1}$. The right panel plots the correlation coefficient between the $(A - B)$ and the final 13 yr maps and demonstrates negligible-to-null correlations, implying that the two maps are independent with the dipole power from the $(A - B)/2$ contributing in quadrature to the signal shown in Figure 3.

Regarding the possibility of systematics, our analysis is not dependent on a precision spectral determination or on an absolute flux, both of which are susceptible to uncertainties in the instrument response. Furthermore, we are not subtracting a Galactic foreground model, which may introduce potential systematics. Finally, our error analysis based on the $A - B$ time differences argues against the presence of time dependencies systematics, which could arise from systematic effects in the exposure maps.

We evaluated the power spectrum of the *dipole- and monopole-removed* source-subtracted 13 yr maps and find it is approximately white out to the computed $\ell = 500$, in agreement with the earlier analyses (Ackermann et al. 2012b, 2018), except about 20%–25% lower because of our (more efficient) source subtraction. The clustering dipole contribution, from averaging the (white) power at $20 < \ell < 500$ to reduce the effects of the cosmic variance at low ℓ , is shown with squares in Figure 3. For the clustering independent of the uncovered dipole, the latter would add in quadrature contributing negligibly in the final dipole balance compared to the found dipole.

The angular uncertainty on the measured γ -ray dipole is shown in Figure 2 for two configurations $|b_{\text{Gal}}| = 30^\circ, 30^\circ \leq l_{\text{Gal}} \leq 330^\circ$ (green contours), and $|b_{\text{Gal}}| = 45^\circ, 45^\circ \leq l_{\text{Gal}} \leq 315^\circ$ (red contours). To estimate the directional uncertainty, we likewise generated $k = 10^4$ random dipoles \mathbf{d}^k with the uncertainties derived from bootstrap. The angular separations between the measured and simulated dipoles sorted in increasing order and the $1\sigma, 2\sigma$ confidence intervals were defined as the regions that encloses 68% and 95% of all angular separations. The uncertainties are marked by the two sets (red and green) of small contours. This dipole determination includes diffuse and time-variable contributions. To estimate the direction and its uncertainty of the diffuse γ -ray component alone, we subtracted the dipole vector $\mathbf{D}_{(A-B)/2}$ from the 13 yr dipole vector $\mathbf{D}_{13 \text{ yr}}$ and added the errors in quadrature. We repeated the procedure as before, and the results are shown by the wider red and green contours. Although the time-varying γ -ray component on the direction has some effect, in the Appendix we show that its effect on the dipole amplitude is negligible. The Pierre Auger dipole is shown as a yellow point, and the arrow indicates its possible location prior to the deflection produced by a model of the Galactic magnetic field.

4. Discussion

Figure 4 summarizes our findings in terms of the dimensionless dipole amplitudes. The identified dipole has dimensionless amplitude $\simeq (6.5\text{--}7)\%$ out to $E \sim 100$ GeV and can be either of Galactic origin or extragalactic from one of the three origins mentioned in Section 1. It is unlikely to come from the Galaxy as its properties show no dependence on the Galactic cuts, $|b_{\text{Gal}}|, l_{\text{Gal}}$, outside of the Galactic center for

$E \gtrsim 3$ GeV. Foregrounds are removed efficiently here, and the DGB is reproduced for the remaining sky as Figure 2 shows.

The dipole directions are consistent for all Galaxy cuts and E configurations with the 68% c.l. errors of $\sim 10^\circ$ – 20° . The rms directional uncertainty is close to $\Delta\Theta \sim \sqrt{2}(S/N)^{-1}$ radian (Fixsen & Kashlinsky 2011). For data in the region $30^\circ \leq l_{\text{Gal}} \leq 330^\circ$ and cuts in $|b_{\text{Gal}}| = 20^\circ, 30^\circ, 45^\circ$, the dipoles are located in the range $(l_{\text{Gal}}, b_{\text{Gal}}) = (-30^\circ \rightarrow \sim 0)$; for the data in the region $45^\circ \leq l \leq 315^\circ$ and for the same cuts in $|b_{\text{Gal}}|$ the dipoles are at Galactic $(l, b) = (270^\circ \rightarrow 300^\circ, -40^\circ \rightarrow 0)$. In Figure 2, we show the direction and its 68% and 95% angular dispersion for two configurations with $30^\circ \leq l \leq 330^\circ$: cuts at $|b_{\text{Gal}}| = 30^\circ$ and $|b_{\text{Gal}}| = 45^\circ$. We note that the direction comparison is further hampered by the deflection of CRs by the Galactic magnetic field, shown by the (model-dependent) location of the UHECR dipole prior to this effect.

We tested for solar system effects, primarily from the Sun and Moon, by removing the ecliptic plane and find no noticeable changes in the dipole as discussed in the Appendix. The distribution of solar system emissions are expected to be sharply distributed about the ecliptic (Johannesson & Orlando 2013). We considered the possibility of γ -ray emission emanating from the solar system by masking the 10° band of the ecliptic plane and find the same signal within the errors, indicating negligible contribution from there demonstrating at most a negligible dipole contribution to the measured signal.

The expected dipole component from clustering, $d_{\text{clustering}}$, is shown in Figure 3 to be on average $\simeq 0.2\%$ from using the power spectra computed here, which is consistent with Ackermann et al. (2012b, 2018); if the found dipole is independent of clustering, $d_{\text{clustering}}$ is added in quadrature, making this contribution totally negligible. Cosmic variance affects the measured clustering dipole per probability distribution $p(d_{\text{clustering}}) = \sqrt{\frac{\pi}{2C_1}} \frac{d_{\text{clustering}}}{C_1} \exp\left(-\frac{d_{\text{clustering}}^2}{2C_1}\right)$ (Kaiser 1983; Abbott & Wise 1984); hence, at 95%, 99% c.l., $d_{\text{clustering}} < 4, 5.7\sqrt{C_1}$, which is still well below the found dipole. This makes clustering an unlikely origin for the measured dipole. The fact that the measured diffuse emission power spectrum agrees well with the other measurements and shows no drastic dependence on the Galaxy cuts further indicates that the diffuse emission, and likely its dipole, do not have critical Galactic components.

If the dipole originates from the Compton–Getting effect due to our kinematic motion, the implied velocity would be $\gtrsim 3000 \text{ km s}^{-1}$, an order of magnitude larger than the CMB dipole equivalent velocity marked with the dashed line in Figure 4 and significantly larger than the effective velocities implied in other dipole measurements (Kashlinsky et al. 2008, 2010, 2011; Singal 2011; Atrio-Barandela et al. 2015; Secrest et al. 2022). Thus, the Compton–Getting amplified kinematic origin of the measured DGB dipole also appears to us implausible.

At face value, there appears a commonality with the UHECR dipole from the Pierre Auger Observatory (Pierre Auger Collaboration et al. 2017). The dimensionless amplitude of the UHECR dipole at $E \gtrsim 3$ EeV is shown in Figure 4 with the solid line at 6.5%. It coincides well with the found DGB dipole, perhaps suggesting a common origin. The source of the UHECRs in general is still unknown. Active galactic nuclei (AGNs) have long been considered as potential sites for production of high-energy CRs, including possibly UHECRs (Fang & Murase 2018; Murase & Stecker 2022).

Also, there has been similar speculation regarding γ -ray bursts (GRBs), and they cannot currently be ruled out as sources of prolific UHECR emission (Murase et al. 2022). However, both of these populations are well known to be highly isotropic. So, some as-yet-identified subpopulation would be required to produce the dipole anisotropy documented by the Pierre Auger experiment if AGNs or GRBs are its source. Very generally, a common origin of UHECR and the [3–100] GeV DGB may be due to pionic photons (Halzen & Hooper 2002) from photomesonic production (Stecker & Salamon 1999) arising in several mechanisms. Possible venues may come from UHECRs above the Greisen–Zatsepin–Kuz’min (GZK) knee around $\sim 10^{20}$ EeV (Greisen 1966; Zatsepin & Kuz’min 1966), with pions arising from the Δ resonance: $p + \gamma_{\text{CMB}} \rightarrow \Delta^+ \rightarrow \pi^0 + p$ or more speculatively from proton decay (Sakharov 1967) $p \rightarrow e^+ + \pi^0$, $p \rightarrow \mu^+ + \pi^0$ (Tanabashi et al. 2018). Subsequently, $\pi^0 \rightarrow 2\gamma$, and on average, the pionic photons would carry $\sim 1/2$ of the parent pion’s energy (Mészáros 2014; Halzen & Kheirandish 2019; Globus & Blandford 2023). GZK horizon of $\lesssim 100$ Mpc would then apply to the sources in the latter case (Stecker 1968; Ding et al. 2021) whose precise value depends on the CR composition (Ahlers & Salvado 2011). The pions trigger electromagnetic cascades, transferring energy from the CRs to the GeV–TeV γ -ray photons (Fornasa & Sánchez-Conde 2015), but their energy flux would have to be up to 50% of the CR flux (Kalashev et al. 2009). However, the dipole here corresponds to the [3–100] flux of $\sim (1-1.5) \times 10^{-7} \text{ GeV cm}^{-2} \text{ s}^{-1} \text{ sr}^{-1}$, which is reached for UHECRs around $E_{\text{UHECR}} \lesssim 1$ EeV (Mészáros 2014; Fang & Murase 2018; Aab et al. 2020b), so it is not clear whether a cascading mechanism can produce the γ -ray signal out of the UHECR protons. More likely this points to a common origin between the CRs and the high- E photons observed here by Fermi-LAT. See possible specific models in, e.g., Waxman (1995); Fang & Murase (2018); Ding et al. (2021). In this case, the distance to the sources may not exceed the horizon for high- E γ -rays (Nikishov 1962; Stecker 1968; Fazio & Stecker 1970) from the CIB and optical background (Kashlinsky 2005b; Helgason & Kashlinsky 2012; Fermi-LAT Collaboration et al. 2018). These sources lie at smaller distances than the cluster sample used in the dark flow dipolar probe (Kashlinsky et al. 2008, 2010) or the source sample of the WISE dipole probe (Secrest et al. 2022) and cannot affect those analyses.

However, as a result of magnetic deflection, using UHECR anisotropy information to constrain the spatial distribution or the nature of the CR sources is not plausible given the limitations inherent in galactic and extragalactic magnetic field models (Allard et al. 2022). Indeed, we cannot unambiguously claim an association between the UHECR and γ -ray dipoles although the coincidence in amplitude and nominal orientation is intriguing. We would note, though, that in the case of a common source, the dipole nature of the UHECR flux is likely to be preserved despite magnetic deflection of individual particles.

In addition to the issue of magnetic deflection it must be considered that the sources of γ -rays and UHECRs may not be strictly in common. For example, it is apparently the case that some subset of γ -ray-emitting blazar AGNs are prolific sources of high-energy neutrinos, while some are not; or perhaps the production sites within the latter are opaque to γ -ray emission

(see, e.g., Plavin et al. 2023). Additionally, there are apparently non-blazar sources of high-energy neutrinos, e.g., NGC 1068 and perhaps the Milky Way itself. The Ice-Cube neutrinos may be unrelated to the Auger UHECRs, but by analogy, the underlying UHCER sources may comprise a similarly nonhomogeneous population.

Acknowledgments

This work was supported by NASA ROSES 2020 grant No. 80NSSC20K1597, “Cosmological Dipole of the Extragalactic Gamma-Ray Background with Multi-Year Fermi LAT Data.” F.A.B. acknowledges financial support from Grants PID2021-122938NB-I00 funded by MCIN/AEI/10.13039/501100011033 and by ERDF “A way of making Europe” and SA083P17 funded by the Junta de Castilla y León. We thank Rick Arendt for careful inspection of the final maps.

Appendix

A.1. Map Clipping

Figure 5 shows the commonality of photons in unclipped maps at the given E between each two adjacent bands starting at 1.15 GeV for the energy range at which the DGB dipole will be assessed. The red/magenta color corresponds to the most photons, with blue corresponding to the fewest. The figure shows that as one reaches higher E , there are fewer and fewer common pixels even among the two most adjacent bands. Figure 6 shows the same after clipping.

A.2. Testing for Null Systematics from the Plane of the Ecliptic

In principle, the Sun produces diffuse γ -rays from the inverse Compton scattering on its radiation field, and the Moon produces some diffuse γ -ray component from CR interactions. Once averaged over the year, the Sun and the Moon may contribute some anisotropic diffuse components contributions, which we test here.

From, e.g., Ackermann et al. (2015), it is evident that the solar system flux can be at a level of up to $\sim 5\%$ of the isotropic background level. However, this emission, which is due to CR interactions with the solar disk and the Moon as well as the inverse-Compton radiation involving the solar radiation field, is concentrated along the ecliptic plane; see, e.g., Figure 2, Johannesson & Orlando (2013). We also generated emission templates as described therein and examined the latitude profiles. Examination of the resulting latitude profiles suggests that a 10° ecliptic latitude cut should lead to eliminating $>90\%$ of the solar system emissions. In any case, the ecliptic latitude cut did not lead to a discernible difference in our dipole determination as noted in Section 4.

Figure 7 shows the same map as used in Sections 2 and 3, Figure 3, demonstrating no obvious contributions from emissions within the ecliptic plane.

Figure 8 shows the dipole/monopole ratio, as in Figure 4, when emissions from the ecliptic plane are not masked out. The two sets of numbers are essentially identical within the errors, demonstrating no substantial contributions to the identified DGB dipole from the solar system and Moon γ -ray emissions.

A.3. Testing for Time Variability with Time-differenced Maps

For estimating the time variations and noise in the maps, we assembled two time-separated subsets of data: subset A for years 1–6 and subset B for years 7–12 with the odd year 13 left out temporarily in this task. The two 6 yr time intervals are each longer than the variability timescales of γ -ray sources. The masks from the clipping of sources and Galaxy for the full 13 yr map in $(b_{\text{Gal}}, l_{\text{Gal}})$ are applied to each subset, and the narrow E -bands are then coadded to produce the 13 band maps going from $E_0 = 2.74$ GeV to the given E up to the final $E = 115$ GeV.

Figure 9 shows the resultant time-differenced map, $(A - B)/2$, with the Galactic plane cut out at $|b_{\text{Gal}}| = 20^\circ$.

Figure 10, left panel, displays the histograms in the time-differenced maps with the ecliptic plane masked out. The source-clipping mask from the full 13 yr data sets has been applied, and the sky is kept at $30^\circ \leq l_{\text{Gal}} \leq 330^\circ$ and $b_{\text{Gal}} \geq 20^\circ$, 30° , 45° for the black/blue/red colors. The standard deviations are shown with vertical solid lines corresponding to $\sigma_{F,(A-B)/2} \sim 1.2 \times 10^{-7} \text{ GeV cm}^{-2} \text{ s}^{-1} \text{ sr}^{-1}$.

Figure 10, right panel, plots the correlation coefficient, $R_{(A-B) \times 13 \text{ yr}}$, between the $(A-B)$ and the final 13 yr maps. The figure demonstrates negligible-to-null correlations, implying that the two maps are independent with the dipole power from the $(A-B)/2$ contributing in quadrature to the signal shown in Figure 3. The precise amplitude, and sign, of the negligible cross correlation appears sensitive to the (small) addition of γ -ray photons at higher E .

Figure 11 shows the ratio of the dipole powers, $C_1 \equiv \langle d_i^2 \rangle$, in the $(A-B)/2$ to that in the 13 yr maps. With the uncorrelated time-varying contribution to the 13 yr dipole added in quadrature, this implies that the dipole power contributed, C_1 , from the time-differenced maps is well below $\lesssim 10\%$. Whereas the 13 yr maps appear to have a stable dipole for the various considered configurations, the $(A - B)/2$ dipole power varies drastically, by more than 2 orders of magnitude, further suggesting the absence of their substantive contributions to the uncovered dipole in Figure 3.

Thus, the time variations between the two 6 yr subsets cannot make appreciable contribution to the dipole power found here.

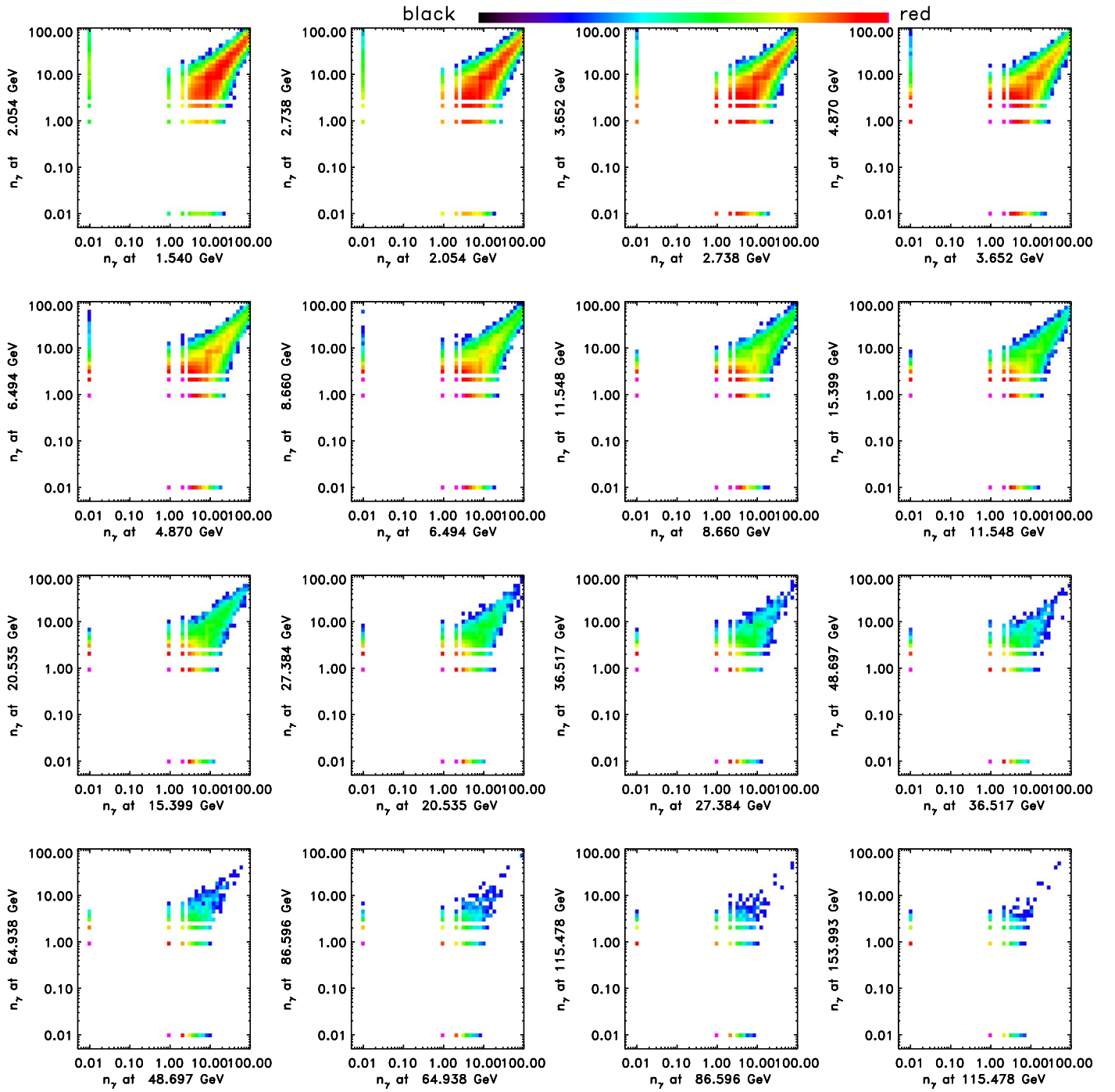


Figure 5. Number of photons per given pixel common in the two adjacent maps is shown with density plots for unclipped maps. The pixels where there are zero photons in one of the two bands are shown at $n_\gamma = 0.01$. The shown colors span 0–5500 common pixels logarithmically.

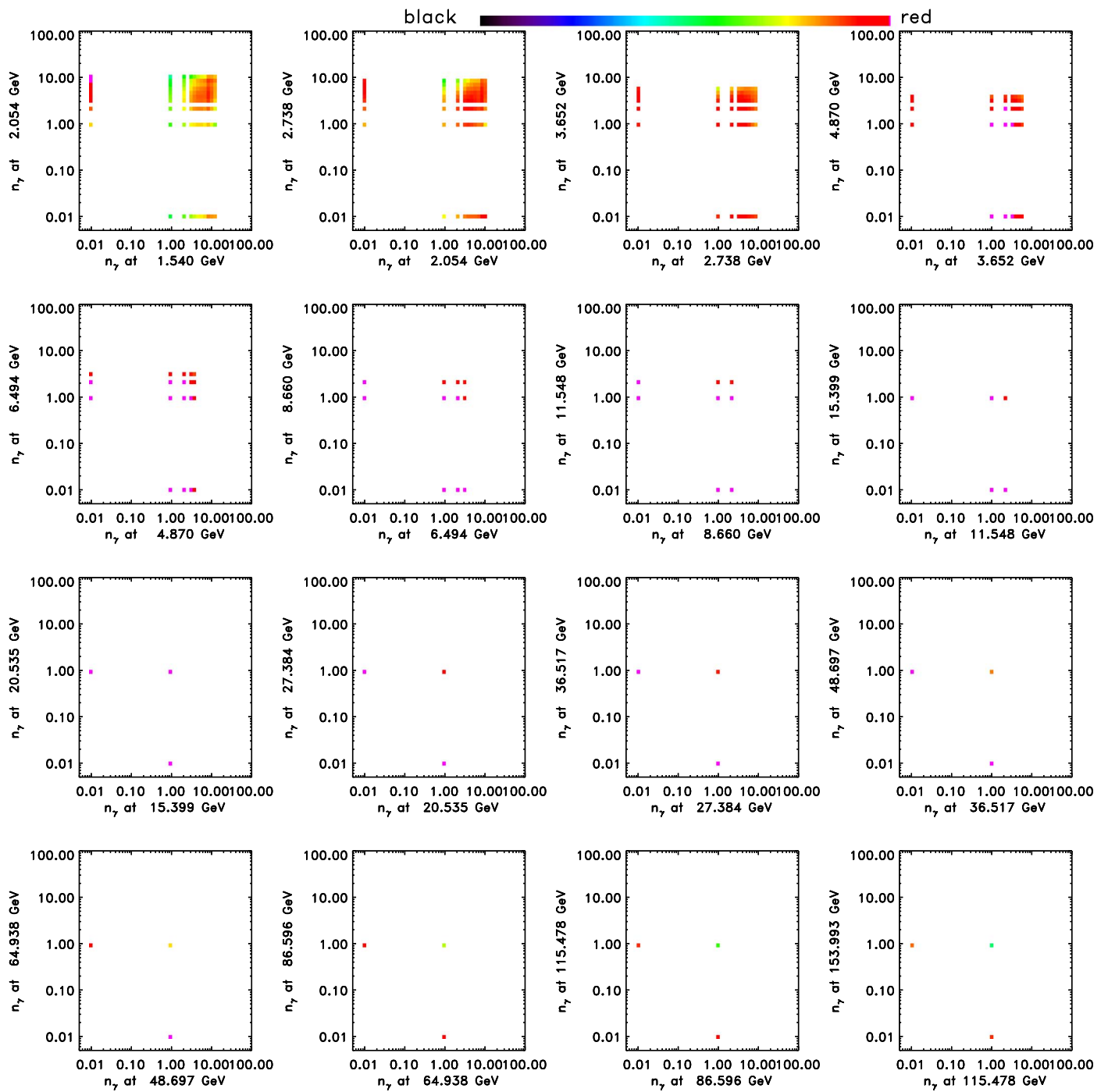


Figure 6. Same as Figure 5 but for clipped maps.

$$2.74 \leq E(\text{GeV}) \leq 115$$

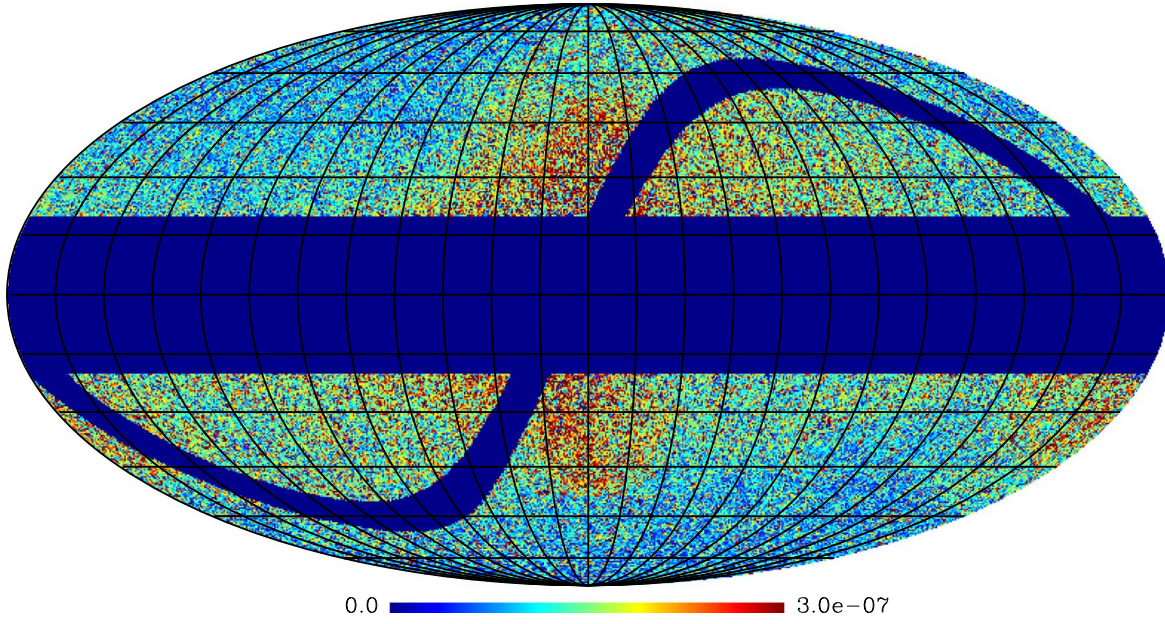


Figure 7. Map with the ecliptic plane masked as in Figure 4 without masking the ecliptic plane.

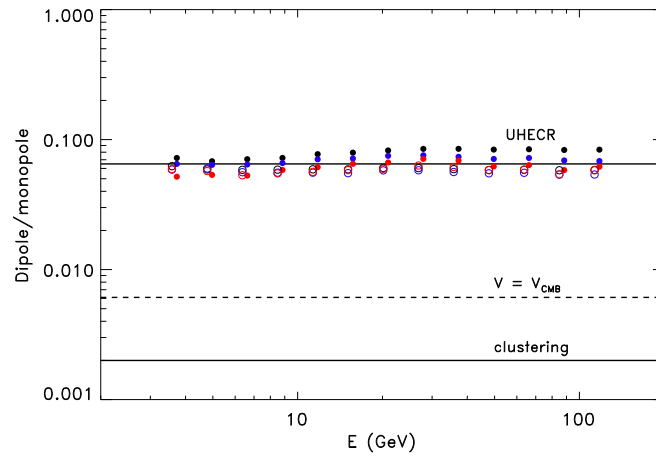


Figure 8. Dimensionless dipole from the maps in Figure 7 in the same notations as in Figure 4 without masking the ecliptic plane. The error bars are barely distinguishable from those in Figure 4 and are not shown to avoid clutter.

$$2.74 \leq E(\text{GeV}) \leq 115.5, (A-B)/2$$

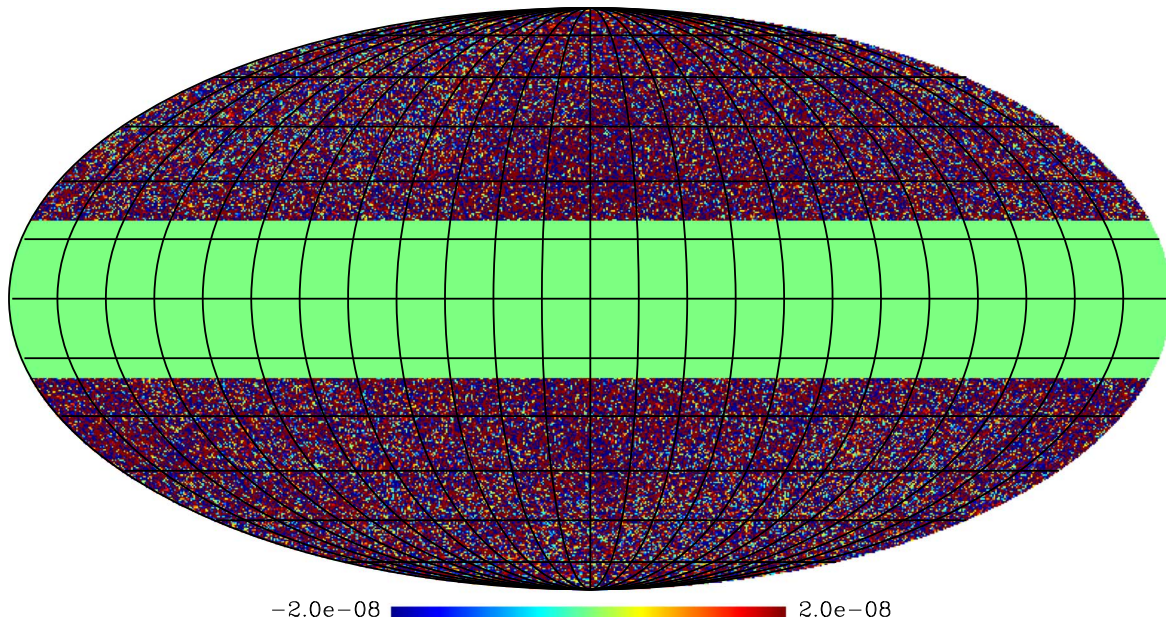


Figure 9. The $(A - B)/2$ map from 2.74 to 115 GeV is shown with the overall 13 yr clipping mask applied and Galaxy removed for $|b_{\text{Gal}}| \leq 20^\circ$.

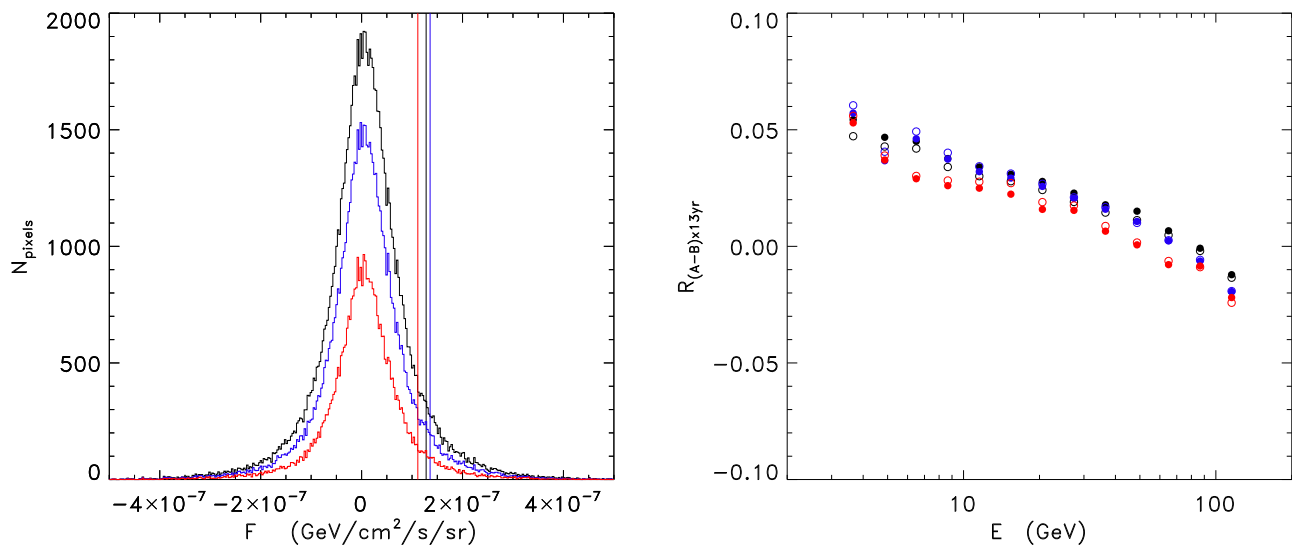


Figure 10. (Left) Histograms of fluxes after the 13 yr clipping mask has been applied to the maps shown in Figure 9. The standard deviations are shown with vertical solid lines corresponding to $\sigma_{F,(A-B)/2} \sim 1.2 \times 10^{-7} \text{ GeV cm}^{-2} \text{ s}^{-1} \text{ sr}^{-1}$. The masking from clipping has been applied, and the sky has been kept at $30^\circ \leq l_{\text{Gal}} \leq 330^\circ$ and $|b_{\text{Gal}}| \geq 20^\circ, 30^\circ, 45^\circ$ for the black, blue, and red colors. (Right) The correlation coefficient, R , between the $(A - B)$ and the final 13 yr maps. Black, red, and blue symbols correspond to $|b_{\text{cut}}| > 20^\circ, 30^\circ, 45^\circ$. The filled and open symbols correspond to $30^\circ \leq l_{\text{Gal}} \leq 330^\circ$ and $45^\circ \leq l_{\text{Gal}} \leq 315^\circ$, respectively.

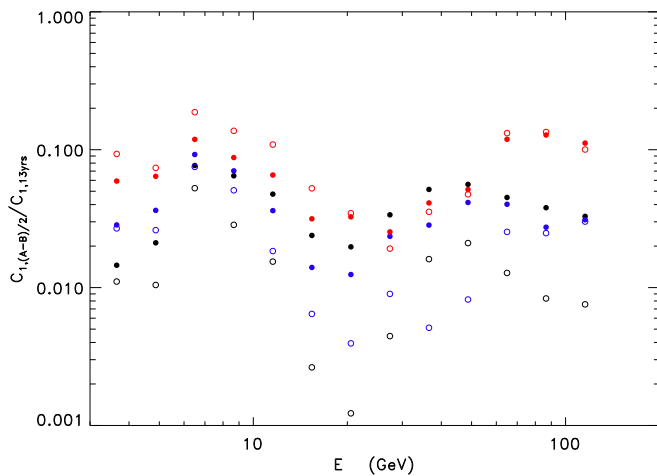


Figure 11. The ratio of the dipole power, $C_1 \equiv \langle d_l^2 \rangle$, in the $(A - B)/2$ to 13 yr maps. Open circles correspond to $45^\circ \leq l_{\text{Gal}} \leq 315^\circ$ and filled to $30^\circ \leq l_{\text{Gal}} \leq 330^\circ$. Black, blue, and red denote $|b_{\text{Gal}}| \geq 20^\circ$, 30° , 45° , respectively.

ORCID iDs

A. Kashlinsky <https://orcid.org/0000-0003-2156-078X>
 F. Atrio-Barandela <https://orcid.org/0000-0002-2130-2513>
 C. S. Shrader <https://orcid.org/0000-0002-0504-549X>

References

- Aab, A., Abreu, P., Aglietta, M., et al. 2020a, *ApJ*, 891, 142
 Aab, A., Abreu, P., Aglietta, M., et al. 2020b, *PhRvD*, 102, 062005
 Abbott, L. F., & Wise, M. B. 1984, *ApJL*, 282, L47
 Abdollahi, S., Acero, F., Baldini, L., et al. 2022, *ApJS*, 260, 53
 Ackermann, M., Ajello, M., Albert, A., et al. 2012a, *PhRvD*, 85, 083007
 Ackermann, M., Ajello, M., Albert, A., et al. 2015, *ApJ*, 799, 86
 Ackermann, M., Ajello, M., Atwood, W. B., et al. 2012b, *ApJ*, 750, 3
 Ackermann, M., Ajello, M., Baldini, L., et al. 2018, *PhRvL*, 121, 241101
 Ahlers, M., & Salvado, J. 2011, *PhRvD*, 84, 085019
 Allard, D., Aublin, J., Baret, B., & Parizot, E. 2022, *A&A*, 664, A120
 Arendt, R. G., Kashlinsky, A., Moseley, S. H., & Mather, J. 2010, *ApJS*, 186, 10
 Atrio-Barandela, F., Kashlinsky, A., Ebeling, H., Fixsen, D. J., & Kocevski, D. 2015, *ApJ*, 810, 143
 Atwood, W. B., Abdo, A. A., Ackermann, M., et al. 2009, *ApJ*, 697, 1071
 Bennett, C. L., Banday, A. J., Gorski, K. M., et al. 1996, *ApJL*, 464, L1
 Bruel, P., Burnett, T. H., Digel, S. W., et al. 2018, arXiv:1810.11394
 Compton, A. H., & Getting, I. A. 1935, *PhRv*, 47, 817
 Ding, C., Globus, N., & Farrar, G. R. 2021, *ApJL*, 913, L13
 Fang, K., & Murase, K. 2018, *NatPh*, 14, 396
 Fazio, G. G., & Stecker, F. W. 1970, *Natur*, 226, 135
 Fermi-LAT Collaboration, Abdollahi, S., Ackermann, M., et al. 2018, *Sci*, 362, 1031
 Fixsen, D. J., Cheng, E. S., Cottingham, D. A., et al. 1994, *ApJ*, 420, 445
 Fixsen, D. J., & Kashlinsky, A. 2011, *ApJ*, 734, 61
 Fornasa, M., & Sánchez-Conde, M. A. 2015, *PhR*, 598, 1
 Globus, N., & Blandford, R. 2023, in EPJ Web of Conf., Ultra High Energy Cosmic Rays (UHECR 2022) 283, ed. I. De Mitri, 04001
 Górski, K. M., Hivon, E., Banday, A. J., et al. 2005, *ApJ*, 622, 759
 Greisen, K. 1966, *PhRvL*, 16, 748
 Halzen, F., & Hooper, D. 2002, *RPPH*, 65, 1025
 Halzen, F., & Kheirandish, A. 2019, *FrASS*, 6, 32
 Helgason, K., & Kashlinsky, A. 2012, *ApJL*, 758, L13
 Johannesson, G., & Orlando, E. 2013, in Proc. ICRC, Accounting for the Sun and the Moon in Fermi-LAT Analysis, 33, ed. A. Saa, 3106
 Kachelrieß, M., & Serpico, P. D. 2006, *PhLB*, 640, 225
 Kaiser, N. 1983, *ApJL*, 273, L17
 Kalashev, O. E., Semikoz, D. V., & Sigl, G. 2009, *PhRvD*, 79, 063005
 Kashlinsky, A. 2005a, *PhR*, 409, 361
 Kashlinsky, A. 2005b, *ApJL*, 633, L5
 Kashlinsky, A., Arendt, R. G., Ashby, M. L. N., et al. 2012, *ApJ*, 753, 63
 Kashlinsky, A., Arendt, R. G., Atrio-Barandela, F., et al. 2018, *RvMP*, 90, 025006
 Kashlinsky, A., & Atrio-Barandela, F. 2022, *MNRAS*, 515, L11
 Kashlinsky, A., Atrio-Barandela, F., & Ebeling, H. 2011, *ApJ*, 732, 1
 Kashlinsky, A., Atrio-Barandela, F., Ebeling, H., Edge, A., & Kocevski, D. 2010, *ApJL*, 712, L81
 Kashlinsky, A., Atrio-Barandela, F., Kocevski, D., & Ebeling, H. 2008, *ApJL*, 686, L49
 Kogut, A., Lineweaver, C., Smoot, G. F., et al. 1993, *ApJ*, 419, 1
 Maoz, E. 1994, *ApJ*, 428, 454
 Mészáros, P. 2014, *NuPhS*, 256, 241
 Murase, K., Mukhopadhyay, M., Kheirandish, A., Kimura, S. S., & Fang, K. 2022, *ApJL*, 941, L10
 Murase, K., & Stecker, F. W. 2022, arXiv:2202.03381
 Nikishov, A. 1962, *JETP*, 14, 393
 Peebles, P. J., & Wilkinson, D. T. 1968, *PhRv*, 174, 2168
 Pierre Auger Collaboration, Aab, A., Abreu, P., et al. 2017, *Sci*, 357, 1266
 Plavin, A. V., Kovalev, Y. Y., Kovalev, Y. A., & Troitsky, S. V. 2023, *MNRAS*, 523, 1799
 Sakharov, A. D. 1967, *JETPL*, 5, 24
 Secrest, N., von Hausegger, S., Rameez, M., Mohayaee, R., & Sarkar, S. 2022, *ApJL*, 937, L31
 Singal, A. K. 2011, *ApJL*, 742, L23
 Smoot, G. F., Bennett, C. L., Kogut, A., et al. 1992, *ApJL*, 396, L1
 Stecker, F. W. 1968, *PhRvL*, 21, 1016
 Stecker, F. W., & Salamon, M. H. 1999, *ApJ*, 512, 521
 Tanabashi, M., Hagiwara, K., Hikasa, K., et al. 2018, *PhRvD*, 98, 030001
 Waxman, E. 1995, *PhRvL*, 75, 386
 Zatsepin, G. T., & Kuz'min, V. A. 1966, *JETPL*, 4, 78